Laser shape variation influence on melt pool dynamics and solidification microstructure in laser powder bed fusion

Li, Erlei; Shen, Haopeng; Wang, Lin; Wang, Geoff; Zhou, Zongyan

DOI
10.1016/j.addlet.2023.100141

Publication date
2023

Document Version
Final published version

Published in
Additive Manufacturing Letters

Additive Manufacturing Letters 6 (2023) 100141

Contents lists available at ScienceDirect

Additive Manufacturing Letters

journal homepage: www.elsevier.com/locate/addlet

Short Communication

Laser shape variation influence on melt pool dynamics and solidification microstructure in laser powder bed fusion

Erlei Li [a,*], Haopeng Shen [b], Lin Wang [c], Geoff Wang [a], Zongyan Zhou [d,e,*]

[a] School of Chemical Engineering, The University of Queensland, St. Lucia 4072, Australia
[b] Manufacturing, CSIRO, Clayton, VIC 3168, Australia
[c] Delft University of Technology, Stevinweg 1, 2628 CN Delft, Netherlands
[d] Department of Chemical and Biological Engineering, Monash University, Clayton, VIC 3800, Australia
[e] International Research Institute for Resources, Energy, Environment and Materials, Jiangxi University of Science and Technology, Nanchang 330013, China

ARTICLE INFO

Keywords:
Laser powder bed fusion
Laser shape variation
Laser incidence angle
Melt pool dynamics
Solidification microstructure

ABSTRACT

The shape variation of the laser beam is evidently observed in the laser powder bed fusion (LPBF) process because of changes in laser incidence angle and misalignment between the build plate and the laser focus plane. This issue is particularly relevant in large-scale LPBF systems where the laser beam needs to scan a large build area. However, most LPBF modeling studies assume vertical laser radiation. The heat transfer, melt pool, and solidification evolution due to the laser shape variation have not been well addressed and quantified. In the present study, the temperature distribution, melt pool geometry and flow dynamics are captured via numerical modelling, and the grain morphology is characterized under various laser incidence angles. The results show that the melt pool depth becomes shallower, and the width is near the beam size as the laser beam becomes more elongated. The beam shape variation can affect the liquid flow pattern with increasing incidence angle, resulting in a larger vortex at the front of the melt pool and a smaller vortex at the rear of the melt pool. The thermal gradient increases and the solidification rate decreases as the laser incident angle becomes larger. The present study enhances the understanding of multi-physics in the LPBF process.

1. Introduction

Laser powder bed fusion (LPBF) fabricates parts layer-upon-layer using laser beams to fuse powder, which is a promising additive manufacturing (AM) technology for metallic production [1,2]. This technology involves a high volume of process parameters [3–5], including laser-related, scanning-related, and powder-related parameters that can affect the microstructure and mechanical properties of the printed products. Understanding the underlying mechanisms behind these parameters allows for better process control and easier parameter optimization to achieve favorable properties in LPBF production. Many studies have been conducted experimentally [6–9] and numerically [10–15] to understand process physics and investigate the effects of various process parameters on the quality of the final parts.

Among various LPBF process parameters, the laser incidence angle has recently attracted great interest since it can lead to quality variations in printed parts [16–18]. The position-dependent laser radiation under different laser incidence angles results in varied power densities for powder melting and further microstructure evolution. For example, the laser beam has a round shape as it is perpendicular to the building platform (usually at the center of the platform), but it becomes oblique at the borders of the platform with elongated elliptical radiation known as laser shape elongation. Because of the distortion of the circle and the varied spot sizes, a position-dependent laser density distribution is produced, resulting in variations in the melt pool. This further can affect the thermal gradient and solidification rate, which can, in turn, affect the solidification microstructure and mechanical properties of the final part.

Optical solutions such as using the F-Theta lens have been applied in state-of-the-art LPBF systems to reduce the shape variation at different building positions. However, a telecentricity error could also create laser distortion and variation of smaller incidence angles on the building plane [18,19]. The beam quality may be compromised to cover a larger printing area, particularly in large-scale machines that push the limit of commercial F-Theta lenses. Another source of laser beam shape variation is the misalignment between the ideal laser focus plane and the actual build plate surface. This issue becomes significant when it is difficult to machine a perfectly flat plate and align it with the fo-

* Corresponding authors.
E-mail addresses: uqeli6@uq.edu.au (E. Li), zongyan.zhou@jxust.edu.cn (Z. Zhou).

https://doi.org/10.1016/j.addlet.2023.100141
Received 25 February 2023; Received in revised form 11 April 2023; Accepted 14 April 2023

cus plane of the F-theta lens, which is particularly relevant in large-scale LPBF systems. The investigation of the laser incidence angle could provide a better understanding of the printing process for such LPBF machines.

The previous studies have attributed the position-dependent surface roughness of printed components due to the laser incidence angles [16–18,20]. For instance, Kleszczynski et al. [18] assumed that the geometrical situation of laser incidence angles causes surface deviations. These different laser incidence angles result from the small inaccuracies of the F-Theta optic. Sendino et al. [17] observed that the surface roughness increases as the test parts' printing positions move from the center to the edge of the building platform. As the distance to the zero-point position (i.e., the incident angle transforms from vertical to inclined) increases, both the surface roughness and porosity increase due to the apparent beam shape change from a circular to an elliptical spot. The latest research has shown that the melt pool dimension and pore defect are related to the laser incidence angle [21–23]. For example, the melt pool width becomes wider, and the depth becomes shallower as the laser moves from the center to the edge, with the laser elongation direction and scan direction being perpendicular [21]. The porosity increases for printed parts with elongated beams due to the decreased laser power intensity [21,22]. Pores are observed at deeper positions in parts that are printed with the more focused laser beam at smaller incidence angles [23].

To the best of the authors' knowledge, a fundamental process understanding of the laser incidence angle through numerical approaches has not been conducted so far in LPBF. Important physics such as how the incidence angle affects the heat transfer, temperature distribution, metallic powder melting, and melt pool dynamics is still unclear. In addition, how the solidification microstructure, which is determined by the thermal gradient and solidification rate, evolves under various laser incidence angles has not been answered. Therefore, a CFD-based model is employed in this work to investigate the influence of the laser incidence angle on heat transfer, powder melting and solidification. The temperature field, melt pool geometry and dynamics are captured under various laser incidence angles. Additionally, the spatial and temporal variation of the thermal gradient and solidification rate is traced. Finally, the impact of the laser incidence angle on the solidification microstructure is addressed. This laser shape variation study can lead to improved control of the microstructure and mechanical properties of LPBF-produced parts.

2. Modelling methodologies

2.1. Model description

In the present work, the discrete element method (DEM) is applied for powder layer spreading first. Then, particle details (e.g., powder size and position) from the previous step are adopted by the CFD method to investigate the laser-powder interaction and subsequent physics of melting and solidification. Details on the powder layer spreading modeling can be found in our previous publications [24,25]. Here, the key features of the CFD model are introduced, which include the Volume of Fluid (VOF), continuity, momentum, and energy equations, as shown in Table 1. For instance, the phases of metal solid, molten liquid, and inert gas are tracked in grid cells by VOF. Key force terms acting on the liquid are considered, such as surface tension, Marangoni force, and recoil pressure. The laser energy, which is usually simplified as the surface or volume heat source in the literature, is represented by the more accurate ray-tracing model with multiple reflections and absorptions. More details about the explanation for equations and model parameters can be found in [26,27]. Compared with our previous studies, the model has been further developed by considering the temperature-dependent physical properties of the material in the present work.

Table 1
Governing equations employed in the modeling melting and solidification of LPBF.

VOF equations:
Liquid phase:
$\partial\alpha_l/\partial t + \nabla\cdot(\alpha_l \boldsymbol{U}) + \nabla\cdot(\alpha_l\alpha_s \boldsymbol{U}_{ls}) + \nabla\cdot(\alpha_l\alpha_g \boldsymbol{U}_{lg}) = (\dot{m}_{sl} - \dot{m}_{ls})/\rho_l$
Solid phase:
$\partial\alpha_s/\partial t + \nabla\cdot(\alpha_s \boldsymbol{U}) + \nabla\cdot(\alpha_s\alpha_l \boldsymbol{U}_{sl}) + \nabla\cdot(\alpha_s\alpha_g \boldsymbol{U}_{sg}) = (\dot{m}_{ls} - \dot{m}_{sl})/\rho_s$
Gas phase: $\frac{\partial\alpha_g}{\partial t} + \nabla\cdot(\alpha_g \boldsymbol{U}) + \nabla\cdot(\alpha_g\alpha_l \boldsymbol{U}_{gl}) + \nabla\cdot(\alpha_g\alpha_s \boldsymbol{U}_{gs}) = 0$
Continuity equation: $\nabla\cdot\boldsymbol{U} = (\dot{m}_{sl} - \dot{m}_{ls})(1/\rho_l - 1/\rho_s)$
Momentum equation:
$\partial(\rho\boldsymbol{U})/\partial t + \nabla\cdot(\rho\boldsymbol{U}\boldsymbol{U}) = -\nabla p + \rho\boldsymbol{g} + \nabla\cdot(\mu(\nabla\mathbf{U} + \nabla\mathbf{U}^T))$
$+C\frac{(1-\alpha_l)^2}{\alpha_l^3 + a}\boldsymbol{U} + \sigma\kappa\nabla\alpha + \frac{d\sigma}{dT}(\nabla T - \boldsymbol{n}(\boldsymbol{n}\cdot\nabla T))\lvert\nabla\alpha\rvert + 0.54P_0 exp\frac{L_v M(T-T_v)}{RTT_v}\nabla\alpha$
Energy equation:
$\partial(\rho C_p T)/\partial t + \nabla\cdot(\rho C_p T\boldsymbol{U}) = \nabla\cdot(k\nabla T) - L_f(\dot{m}_{sl} - \dot{m}_{ls}) +$
$+S_{laser}$

2.2. Simulation conditions

The dimensions of the computational domain at the X, Y and Z axes are 1000 μm, 440 μm and 370 μm, respectively. The powder layer is filled with titanium alloy (Ti-6Al-4V) particles at a thickness of 70 μm. The laser scans a single track along the centerline (Y = 220 μm) with a length of 800 μm. The temperature-dependent material properties of Ti-6Al-4V [28,29], such as density, thermal conductivity and heat capacity, are listed in Table 2. The boundary conditions, sensitivity test of mesh resolution, and algorithm to compute the model variables have been discussed in detail in previous works [26]. The depth of the melt pool is the averaged dimension along the Z axis. The melt pool width is the averaged dimension along the Y axis. The scanned powder bed regions in all cases are the same in this work.

2.3. Laser shape variation

The laser shape variation can arise due to changes in the laser incidence angle and the misalignment between the build plate and the laser focus plane, as illustrated in Figs. 1(a) and (b). To explore the effects of the laser beam variation, laser incidence angles ranging from 60° to 120° were employed in this work. The projection of a circular beam on the powder bed turns into an elliptic shape, as presented in Fig. 1(c), and the direction of the shape elongation is parallel to the laser scan direction. The laser beam length in elongation is calculated based on the diagram of Fig. 1(a), where $d_l = \frac{d}{\sin\theta}$. It first falls and then grows as the laser incidence angle increases from 60° to 120° (see Table 3 for the specified values of the laser length in elongation). This gives the maximum beam aspect ratio to 1.15, where $\alpha = \frac{d_l}{d}$. The laser spot area projected onto a plane displays the same tendency as the laser elongation length during the variation of laser incidence angles. The laser power density [30], defined as the ratio of the laser power to the laser spot area ($P_l = \frac{P}{A_l}$), drops by 13.40% as the laser rays at 90° incline to either 60° or 120°. The laser interaction time here indicates the ratio of the laser length to the scanning speed ($t_l = \frac{d_l}{v}$) [31]. The laser angles of 60° and 120° present the longest laser interaction times due to shape distortion. Although the laser incidence angles lead to variations in the powder density and interaction time, the total energy density ($E_l = P_l t_l$) [31] remains constant for the five different laser incidence angles, as shown in Table 3. The angle of incidence and the way it interacts with the sample are illustrated in Fig. 1(d) in the simulation.

2.4. Solidification microstructure

The tail of the melt pool solidifies as the laser moves forwards as presented in Fig. 2(a), and the temperature of the rear melt pool decreases

Table 2
Material properties and process parameters employed in the present work [28,29].

Items	Values
Density of solid (ρ_s, kg m^{-3})	$4420 - 0.154(T - 298)$
Density of liquid (ρ_l, kg m^{-3})	$3920 - 0.68(T - 1923)$
Specific heat capacity of solid (C_{ps}, J kg^{-1} K^{-1})	$\begin{cases} 483.04 + 0.215T & T \le 1268K \\ 412.7 + 0.1801T & 1268K < T \le 1923K \end{cases}$
Specific heat capacity of liquid (C_{pl}, J kg^{-1} K^{-1})	831.0
Thermal conductivity of solid (k_s, W m^{-1} K^{-1})	$\begin{cases} 1.2595 + 0.0157T; & T \le 1268\ K \\ 3.5127 + 0.0127T; & 1268\ K < T \le 1923K \end{cases}$
Thermal conductivity of liquid (k_l, W m^{-1} K^{-1})	$-12.752 + 0.024T$
Dynamic viscosity of liquid (μ_l, kg m^{-1} s^{-1})	3.25×10^{-3} (1923 K); 3.03×10^{-3} (1973 K); 2.66×10^{-3} (2073 K); 2.36×10^{-3} (2173 K)
Latent heat of fusion (L_f, J kg^{-1})	2.86×10^5
Latent heat of vaporization (L_v, J kg^{-1})	9.83×10^6
Surface tension (σ, kg s^{-2})	1.5
Surface tension gradient ($d\sigma/dT$, kg s^{-2} K^{-1})	-2.8×10^{-4}
Solidus temperature (T_s, K)	1877
Liquidus temperature (T_l, K)	1923
Boiling temperature (T_v, K)	3533
Laser power (P, W)	150
Scan speed (v, mm s^{-1})	1000
Laser beam diameter (d, μm)	100

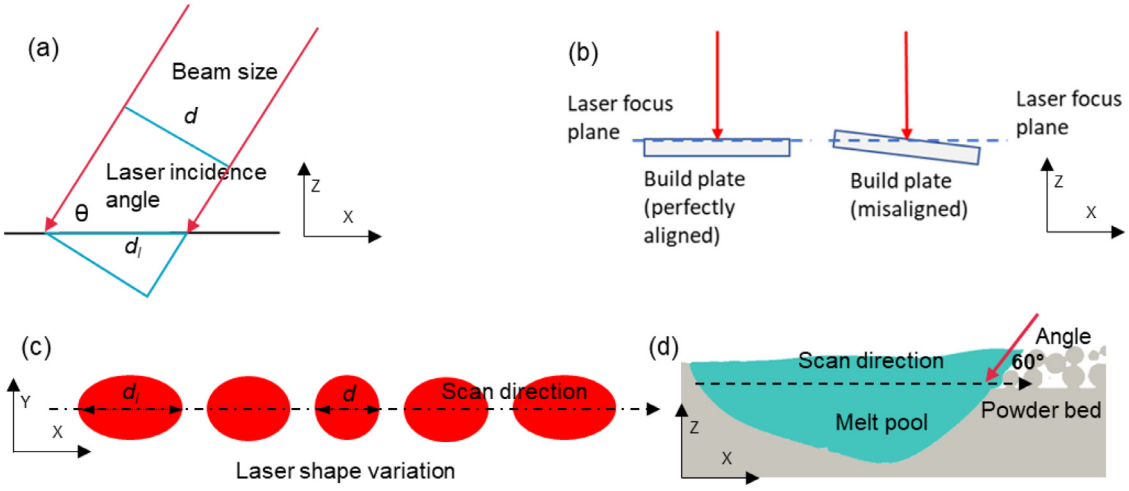

Fig. 1. Schematic diagram of laser shape variation: (a) the interaction between inclined laser beams and the powder bed; (b) misalignment of the build plate plane; (c) the projection of a circular beam on a plane with shape elongation; and (d) illustration of angle of incidence and the way it interacts with the sample (the laser incidence angle of 60° presented here).

Table 3
Influence of laser incidence angle on beam energy deposition.

Incidence angle (θ, °)	Laser beam length† (d_l, μm)	Beam aspect ratio (α)	Laser spot area (A_l, μm^2)	Power density (P_l, kW/mm^2)	Interaction time (t_l, μs)	Energy density (E_l, J/mm^2)
60	115.47	1.15	9064.40	16.55	115.47	1.91
75	103.53	1.04	8126.92	18.46	103.53	1.91
90	100.00	1.00	7850.00	19.11	100.00	1.91
105	103.53	1.04	8126.92	18.46	103.53	1.91
120	115.47	1.15	9064.40	16.55	115.47	1.91

† Laser beam diameter is kept constant at 100 μm.

towards the solidification front at the solid–liquid interface. First, the temperature field of the trailing solid–liquid interface is extracted, as shown in Fig. 2(b). Then, the thermal gradient and solidification rate at the solidifying interface are calculated to evaluate the solidification microstructure. Specifically, the thermal gradient, which is the magnitude of the temperature field gradient [32,33], is expressed as follows:

$$G = |\nabla T| = \sqrt{\left(\frac{\partial T}{\partial x}\right)^2 + \left(\frac{\partial T}{\partial y}\right)^2 + \left(\frac{\partial T}{\partial z}\right)^2} \quad (1)$$

where G is the thermal gradient and T is the temperature.

The solidification rate is expressed as [32,33]

$$R = v\frac{|\partial T/\partial x|}{G} \quad (2)$$

where R and v are the thermal gradient and laser scan speed, respectively.

The grain morphology regions are based on an analytical model developed by Hunt [34]. The extracted G and R values at the solidifying interface are plotted on a reference Ti-6Al-4V solidification map to characterize the grain structures. This solidification map of Ti-6Al-4V was experimentally established by Kobryn et al. [35] and has been applied in numerical studies [36]. In the solidification map, the prior-beta

Table 4
Simulation of average melt pool width and depth compared to experimental results.

Process parameters	Melt pool width (μm)			Melt pool depth (μm)		
	Experiment	Simulation	Error (%)	Experiment	Simulation	Error (%)
200 W, 1200 mm/s	111	119	7.21	–	–	–
300 W, 1000 mm/s	172	150	−12.79	155	169	9.03
300 W, 1200 mm/s	153	137	−10.46	120	135	12.5

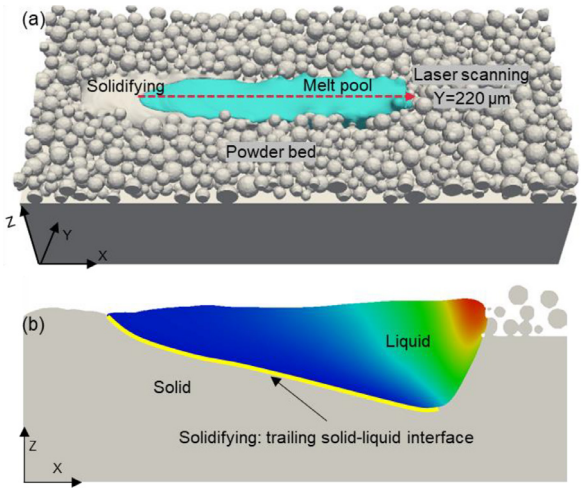

Fig. 2. (a) Melting and solidifying process and (b) schematic diagram of the solidification interface, indicated by the yellow line, for computing the solidification rate and thermal gradient.

grain morphology can be characterized as fully equiaxed, mixed, or fully columnar based on the G and R values. Therefore, the influence of laser incidence angles on the solidification microstructure can be predicted in the present work.

2.5. Model validation

The model used in the present work has been well-validated by experimental data in our previous work [26,27,37]. For instance, the simulated melt pool dimensions and part surface roughness agree well with experimental results [26]. In addition, the melt pool flow dynamics obtained from the simulation is consistent with the experimental observations [27]. Additionally, the keyhole depth and morphologies match the experimental data well [37]. The model is further validated in this study since the temperature-dependent thermal properties are introduced. In this study, the simulated melt pool width and depth are further compared with the experimental results. Note that the melt pool depth here is measured from the substrate surface to the deepest rim along the Z axis. The comparison results, as presented in Table 4, show that the simulated width and depth have good agreement with experimental points [38] with a maximum error of −12.79%. The tendency of melt pool dimensions after laser elongation will be explained in Section 3.1, where a comparison between simulation and experiments will be made. Overall, these results demonstrate the reliability of this model in simulating the heat diffusion, temperature field, melt pool dynamics and solidification.

3. Results and discussion

3.1. Melt pool temperature and geometry

Since the total energy density is constant in varied incidence angles (discussed in Section 2.3), how the absorptivity performs under these conditions determines the powder melting and melt pool temperature. Therefore, the effect of incidence angle on the laser absorptivity is examined. The simulation cases are carried out under the conditions as shown in Fig. 1(d), where the laser interacts with the powder and melt pool under different laser incidence angles. Here, the absorptivity ratio (i.e. the ratio of absorptivity at any incidence angle to that under 90-degree case) is adopted to compare the varied laser absorptivity, as shown in Fig. 3(a). The absorptivity is found to be comparable and shows a slight increase as the 90-degree laser beams become inclined to the build plate plane. This is consistent with literature data [39]. It indicates that both the deposited and distributed heat source on the powder bed is close under the conditions of 60° to 120°. In the present study, the keyhole or vapor depression is ignored. The generation of a vapor cavity can affect the dynamics of the laser-material interaction as multi-reflections of the laser beam occur in the depression zone. This can enhance the laser energy adsorption and further affect the temperature, melt pool dynamics, and microstructure. Further work should be carried out to analyze to what extent the laser angle affects the laser-material interaction under the depression conditions.

Next, the melt pool temperature at different laser incidence angles is presented in Fig. 3(b). Noted that the laser scans from the same location in all simulated cases, and the temperature curve starts from different positions due to the variation in the laser incidence angle. The temperature curve along the scan path displays a trend that increases gradually and finally falls slightly. The peak point of the temperature should be at the laser beam center, and therefore, the temperature declines in front of the laser center. Regarding the effect of laser shape variation, the maximum value decreases as the laser beam turns from the angle of 60° to the vertical position. The temperature curves are similar for larger incidence angles. When the laser beam is applied to heat the molten liquid at an angle of 60°, it presents the highest temperature. For larger incidence angles, the laser energy is diffused to the cold powder particles. Therefore, the maximum temperature point is lower than that at the angle of 60°.

Then, the influence of laser shape variation on the melt pool width and depth is explored and presented in Fig. 3(c). The melt pool width decreases slightly first and then increases as the laser incidence angle varies from 60° to 120° The laser beam diameter perpendicular to the scan direction is equivalent for all five cases. Hence, the heat diffusion along the melt pool width direction is similar, which contributes to the similar melt pool widths. This trend of the melt pool width is consistent with that was observed in the experiment [22], where the shape elongation direction is parallel to the scan direction, despite the different materials employed. The melt pool depth falls from 162 μm to 152 μm as the laser incidence angle changes from 60° to 120°. Note that the depth here refers to the average maximum dimension along the Z-axis, where the depth of the melted powder layer and the depth of the melted solid layer are both included. In addition to the heat diffusion along the Z-axis of the computational domain, the energy also accelerates to the high-temperature liquid (particles that have been melted) along the negative X-axis at the shape elongations of 60° and 75°. This kind of head diffusion is opposite to the scan direction, which is along the positive X-axis. The heat spreads forwards to the frozen solid along the positive X-axis under the shape elongations of 105° and 120°. This leads to melt pool depth difference where the melt pool depth decreases continuously.

The melt pool shape, defined as the ratio of the width to the depth of the melt pool, is presented in Fig. 3(d). The melt pool width-to-depth

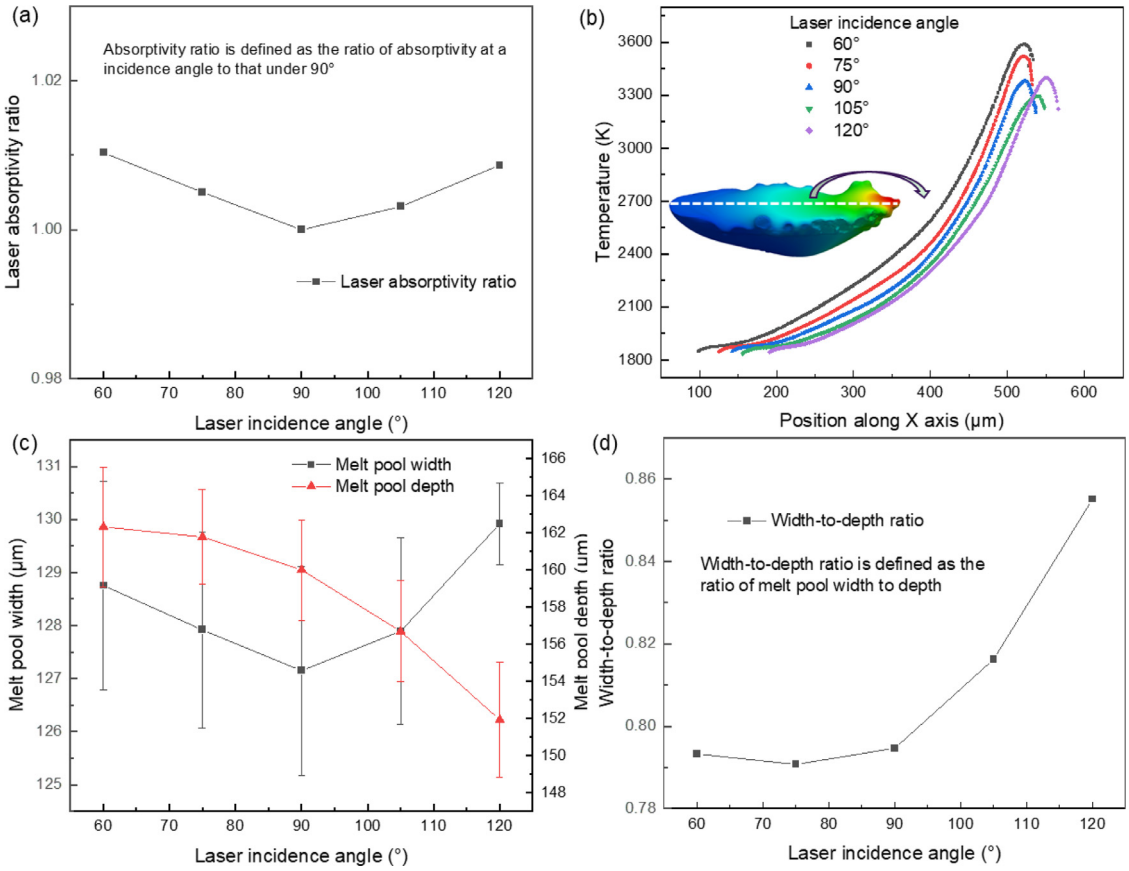

Fig. 3. The effects of laser incidence angle on (a) laser absorptivity ratio; (b) temperature distribution along the laser scan path (at $Y = 220$ μm and $t = 430$ μs); (c) melt pool width and depth; and (d) melt pool shape. The process parameters are laser power 150 W, scanning speed 1000 mm/s and laser spot 100 μm.

ratio is almost the same, approximately 0.79, under the operating conditions where the laser shape incidence angle is less than or equal to 90°, and the laser beam is perpendicular to the building platform. It increases to 0.86 as the laser incidence angle grows to 120°, indicating that the melt pool shape is flatter at the higher laser incidence angle due to the decreased melt pool depth.

3.2. Melt pool flow dynamics

When the laser beam is projected at small incidence angles (i.e., 60° and 75°), heat diffusion takes priority along the negative X-axis, which is opposite to the scan path. The high-temperature region is almost symmetrical to the cooling area shown in Fig. 4(a), where regions are distinguished by the dashed white line. As the laser shape elongation moves from 60° to 120°, the deposited laser energy accelerates the heat spreading in the same direction of the scan path (i.e., along the positive X-axis). Therefore, the front high-temperature region becomes larger, and a more inclined melt pool is generated (see Figs. 4(a)-(e)). The maximum depth of the melt pool shifts from the middle to the front part due to the spatial laser density distribution. Additionally, the solidification interface becomes longer as the laser incident angle increases.

At a low incidence angle, one large anticlockwise vortex and one small clockwise vortex are developed, as shown in Fig. 4(a). Since the heat diffusion is mainly directed backwards, the high temperature gradient largely occurs at the rear of the laser beam. Hence, the Marangoni force caused by the thermal gradient drives the hot liquid to the low-temperature region at the interface. It further flows forwards inside the molten liquid, and a large vortex is thus produced. The thermal gradient at the front of the melt pool results in the formation of a small vortex. The comparable size of one anticlockwise and one clockwise vortex occurs at the circular beam, which has been revealed in previous work [40]. The region of the front clockwise becomes larger and the anticlockwise decreases as the laser incidence angle increases. This is because the forwards heat diffusion dominates the energy deposition, contributing to the distinct thermal gradient at the front of the melt pool. As a result, a relatively large clockwise vortex is developed (see Fig. 4(e)). In summary, the variation distribution of the laser intensity on the projection plane leads to the variation of the temperature field and temperature gradient (i.e., Marangoni force), which further contributes to different flow patterns. The flow dynamics will further affect the temperature and melt pool characteristics, which has been well discussed in the literature [41–43]. In the present work, the effects of laser incidence angle are investigated. For instance, the large anticlockwise vortex at the rear region of the melt pool at an incidence angle of 60° carries the low-temperature liquid to the high-temperature region. This leads to a wider melt pool and more uniform temperature distribution at the solidification interface. The dominant flow transfers from anticlockwise to clockwise with increasing incidence angle, which contributes to the higher thermal gradient at the trailing solid-liquid interface.

3.3. Microstructure morphology

The values of the temperature gradient and solidification rate at the solidification interface of the melt pool were calculated based on the methods described in Section 2.4. Note that the thermal gradient and solidification rate vary spatially within the melt pool, and their distribution is presented in Fig. 5(a). The thermal gradient increases from the center to the border, which is in the order of 10^6 K/m. Since the edge molten liquid is close to the cool solid, a high thermal gradient exists in these regions. The solidification rate displays the opposite trend

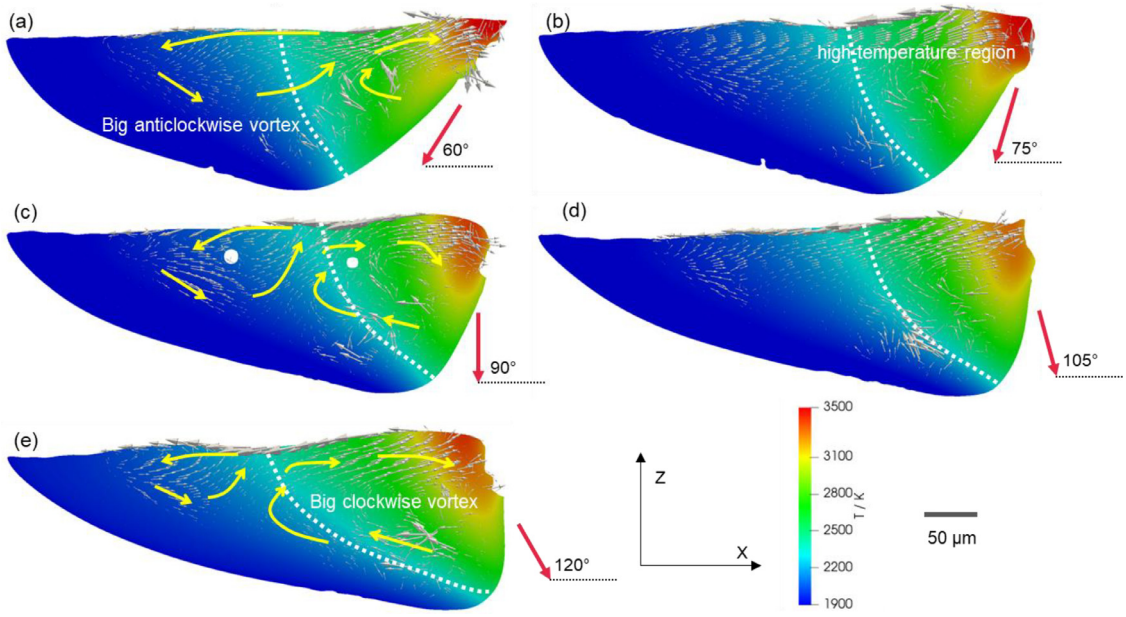

Fig. 4. Temperature field, melt pool geometry and flow patterns versus laser shape variation, (a)-(e) correspond to laser incidence angles of 60˚, 75˚, 90˚, 105˚ and 120˚, respectively. The cross-section is obtained along the laser scan path at $Y = 220$ μm at $t = 430$ μs.

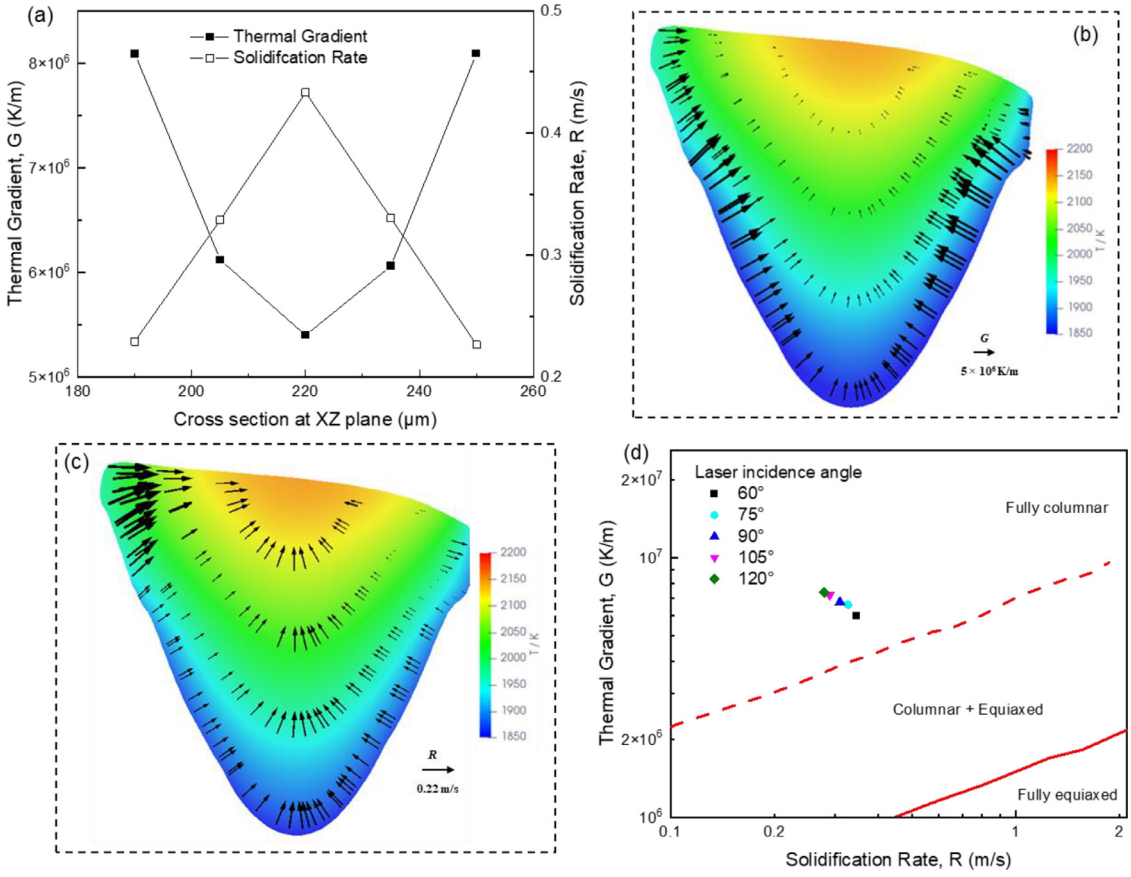

Fig. 5. (a) Spatial distribution of the temperature gradient and solidification rate under 90-degree laser radiation; (b) and (c) are temporal temperature gradient and solidification rate at the cross section of the melt pool, respectively (the vector arrow and length indicate the direction and magnitude, respectively). The specific timelines are 500, 600, 700 and 800 μs as the solidification interface moves from the bottom to the top of the melt pool; and (d) solidification microstructure under various incidence angles. The average spatial and temporal temperature gradient and solidification rate are adapted here.

to the thermal gradient, which decreases from the center to the edge of the melt pool. The value of the solidification rate is in the order of 10^{-1} m/s. The spatial variation of thermal gradient and solidification rate at the solidification interface could lead to the grain structure or size difference in the solidified microstructure. This results in the change of mechanical properties at different positions in printed components.

In addition to the spatial difference, the temporal distribution of temperature gradient and solidification rate also varies. Here, data points at four time series are adopted to capture their changes. The temperature gradient decreases dramatically from the edge to the center as the molten liquid gradually solidifies, as displayed in Fig. 5(b). Besides, the side presents a higher value of temperature gradient than that at the bottom of the solidifying interface. The solidification rate drops quickly at the primary stage of solidification (i.e., 500 to 600 μs) while it remains close at the final period (700 to 800 μs), as shown in Fig. 5(c).

As the temperature gradient and solidification rate vary in space and time, the average spatial and temporal values are calculated. The result of the effect of laser incidence angle on prior-beta grain morphology is presented in Fig. 5(d). The solidification microstructure for all laser incidence angles falls in the fully columnar region. However, the *G-R* points move to the top upper area as the laser incident angle becomes larger, which indicates that the thermal gradient increases and the solidification rate decreases. For instance, the value of *G* varies from 5.96×10^6 K/m to 7.36×10^6 K/m as the angle increases from 60° to 120°. The *R* points range from 0.35 m/s to 0.28 m/s at the observed laser incidence angles.

3.4. Discussion

The inclined laser produces an elongated elliptical beam profile on the projection plane. As a result, the increased laser spot area leads to the decreased powder density, e.g., a 13.40% reduction at laser incidence angles of 60° or 120° compared to the 90-degree laser rays. Additionally, in this study, when the direction of the laser shape elongation is parallel to the scan direction, the energy density remains constant due to the simultaneously increased interaction time. Besides, the absorptivity among various used laser incidence angles is comparable. Therefore, the melt pool width is close under various angles. However, the subordinate heat diffusion directs to the high-temperature molten liquid under angles of 60° and 75°, which deepens the melt pool dimension. In contrast, the heat is partially diffused to the cold solid powders at the melting front at laser incidence angles of 105° and 120°, which causes a shallower melt pool depth. Consequently, the maximum temperature of the melt pool decreases as the laser beam turns from the angle of 60° to vertical.

Backward laser irradiation (i.e., the small laser incidence angle of 60°) generates a large anticlockwise vortex at the rear region of the melt pool, which carries a larger amount of low-temperature liquid to the high-temperature region. This kind of flow dynamics leads to a more uniform temperature distribution at the solidification interface. Hence, a low thermal gradient is generated, as shown in Fig. 5(d). On the other hand, the forward laser projection (i.e., large laser incidence angle of 120°) forms a small anticlockwise vortex at the rear melt pool, indicating week heat exchange at the back of the melt pool. In addition, the front large clockwise vortex only stirs the high-temperature liquid. As a result, a higher thermal gradient at the trailing solid-liquid interface is produced compared to the backward laser radiation.

A strong columnar grain structure of Ti-6Al-4V is fabricated by laser powder bed fusion in this study, which agrees well with experimental observations and knowledge [44–46]. The spatial and temporal variations in the thermal gradient and solidification rate are both related to thermal physics. Although the center of the melt pool is radiated directly by the laser beams, the temperature gradient is low as the heat has been fully diffused through the melt pool. In contrast, the edge of the melt pool is close to the cold solid, which produces a high thermal gradient. The columnar grains are usually coarse, and this columnar macrostructure leads to anisotropic material properties, such as tensile strength [47–49]. For a large-scale LPBF printer, a low thermal gradient and a high solidification rate could be achieved by selecting small incidence angles.

4. Conclusions

In this work, the influence of laser shape variation caused by the laser incidence angle on heat transfer, melt pool geometry and dynamics, and solidification microstructure are revealed by numerical modeling. The key findings are concluded as follows:

(1) The power density decreases by up to 13.40% as the 90-degree laser rays incline to 60° or 120°. The energy density remains constant under various incidence angles due to the simultaneously increased interaction time. The absorptivity is comparable for the employed laser incidence angles.
(2) The melt pool width is close, while the depth becomes shallower as the laser incidence angle increases from 60° to 120°. The increase in the laser incidence angle enlarges the melt pool width-to-depth ratio. The maximum value of the melt pool temperature decreases as the laser beam turns from the angle of 60° to the vertical position.
(3) The front high-temperature region becomes larger, and a more inclined melt pool is generated at the angle of 120°. With increasing incidence angles, the anticlockwise vortex at the rear of the melt pool decreases, and the front clockwise vortex becomes larger due to the different directions of laser radiation and heat diffusion.
(4) The thermal gradient increases, and the solidification rate decreases from the center to the border of the melt pool, and both decline as the melt pool gradually solidifies. A strong columnar grain structure is achieved under the five different laser incidence angles. The thermal gradient increases, and the solidification rate decreases as the laser incident angle becomes larger.

It is worth noting that this study ignores the vapor cavity. The temperature, melt pool geometry, flow pattern and microstructure evolution under the keyhole condition will be explored in the future, as the vapor depression could affect the results significantly. Additionally, in this work, the laser shape elongation direction is parallel to the scan direction. The perpendicular cases should also be simulated in the future to cover the full picture of thebuilding platform.

Declaration of Competing Interest

The authors declare that they have no known competing financial interests or personal relationships that could have appeared to influence the work reported in this paper.

Data availability

No data was used for the research described in the article.

Acknowledgements

The authors are grateful for the financial support from the Australian Research Council Industrial Transformation Research Hubs Scheme (Project Number IH140100035). This research was undertaken with the assistance of supercomputing resources from the Pawsey and National Computational Infrastructure (NCI), which are supported by the Australian Government.

References

[1] W.E. Frazier, Metal additive manufacturing: a review, J. Mater. Eng. Perform. 23 (2014) 1917–1928.
[2] W.J. Sames, F.A. List, S. Pannala, R.R. Dehoff, S.S. Babu, The metallurgy and processing science of metal additive manufacturing, Int. Mater. Rev. 61 (2016) 315–360.
[3] I. Gibson, D.W. Rosen, B. Stucker, M. Khorasani, D. Rosen, B. Stucker, M. Khorasani, Additive Manufacturing Technologies, Springer, 2021.

[4] E. Li, Z. Zhou, L. Wang, R. Zou, A. Yu, Particle scale modelling of powder recoating and melt pool dynamics in laser powder bed fusion additive manufacturing: a review, Powder Technol. (2022) 117789.
[5] N.T. Aboulkhair, N.M. Everitt, I. Ashcroft, C. Tuck, Reducing porosity in AlSi10Mg parts processed by selective laser melting, Addit. Manuf. 1 (2014) 77–86.
[6] H. Gong, K. Rafi, H. Gu, G.D.J. Ram, T. Starr, B. Stucker, Influence of defects on mechanical properties of Ti–6Al–4V components produced by selective laser melting and electron beam melting, Mater. Des. 86 (2015) 545–554.
[7] S. Zhang, Q. Wei, L. Cheng, S. Li, Y. Shi, Effects of scan line spacing on pore characteristics and mechanical properties of porous Ti6Al4V implants fabricated by selective laser melting, Mater. Des. 63 (2014) 185–193.
[8] K. Wei, F. Li, G. Huang, M. Liu, J. Deng, C. He, X. Zeng, Multi-laser powder bed fusion of Ti–6Al–4V alloy: defect, microstructure, and mechanical property of overlap region, Mater. Sci. Eng. 802 (2021) 140644.
[9] Y. Huang, T.G. Fleming, S.J. Clark, S. Marussi, K. Fezzaa, J. Thiyagalingam, C.L.A. Leung, P.D. Lee, Keyhole fluctuation and pore formation mechanisms during laser powder bed fusion additive manufacturing, Nat. Commun. 13 (2022) 1–11.
[10] H.L. Wei, Y. Cao, W.H. Liao, T.T. Liu, Mechanisms on inter-track void formation and phase transformation during laser powder bed fusion of Ti-6Al-4V, Addit Manuf 34 (2020).
[11] C. Meier, R. Weissbach, J. Weinberg, W.A. Wall, A.J. Hart, Critical influences of particle size and adhesion on the powder layer uniformity in metal additive manufacturing, J. Mater. Process. Technol. 266 (2019) 484–501.
[12] A.U. Rehman, M.A. Mahmood, F. Pitir, M.U. Salamci, A.C. Popescu, I.N. Mihailescu, Keyhole formation by laser drilling in laser powder bed fusion of Ti6Al4V biomedical alloy: mesoscopic computational fluid dynamics simulation versus mathematical modelling using empirical validation, Nanomaterials 11 (2021).
[13] E. Li, Z. Zhou, L. Wang, Q. Zheng, R. Zou, A. Yu, Melt pool dynamics and pores formation in multi-track studies in laser powder bed fusion process, Powder Technol. 405 (2022) 117533.
[14] Y. Huang, M.B. Khamesee, E. Toyserkani, A new physics-based model for laser directed energy deposition (powder-fed additive manufacturing): from single-track to multi-track and multi-layer, Opt. Laser Technol. 109 (2019) 584–599.
[15] K.Q. Le, C. Tang, C.H. Wong, On the study of keyhole-mode melting in selective laser melting process, Int. J. Therm. Sci. 145 (2019).
[16] S. Rott, A. Ladewig, K. Friedberger, J. Casper, M. Full, J.H. Schleifenbaum, Surface roughness in laser powder bed fusion–Interdependency of surface orientation and laser incidence, Addit. Manuf. 36 (2020) 101437.
[17] S. Sendino, M. Gardon, F. Lartategui, S. Martinez, A. Lamikiz, The effect of the laser incidence angle in the surface of l-pbf processed parts, Coatings 10 (2020) 1024.
[18] S. Kleszczynski, A. Ladewig, K. Friedberger, J. zur Jacobsmühlen, D. Merhof, G. Witt, Position dependency of surface roughness in parts from laser beam melting systems, 2015 International Solid Freeform Fabrication Symposium, University of Texas at Austin, 2015.
[19] Benedikt Brandau, Spectral Analysis in Laser Powder Bed Fusion, Luleå University of Technology, 2022.
[20] Z. Chen, X. Wu, C.H.J. Davies, Process variation in laser powder bed fusion of Ti-6Al-4V, Addit. Manuf. 41 (2021) 101987.
[21] P. Fathi-Hafshejani, A. Soltani-Tehrani, N. Shamsaei, M. Mahjouri-Samani, Laser incidence angle influence on energy density variations, surface roughness, and porosity of additively manufactured parts, Addit. Manuf. 50 (2022) 102572.
[22] T. Fiegl, M. Franke, C. Körner, Impact of build envelope on the properties of additive manufactured parts from AlSi10Mg, Opt. Laser Technol. 111 (2019) 51–57.
[23] K. Tsubouchi, T. Furumoto, M. Yamaguchi, A. Ezura, S. Yamada, M. Osaki, K. Sugiyama, Evaluation of spatter particles, metal vapour jets, and depressions considering influence of laser incident angle on melt pool behaviour, Int. J. Adv. Manuf. Technol. 120 (2022) 1821–1830.
[24] L. Wang, E.L. Li, H. Shen, R.P. Zou, A.B. Yu, Z.Y. Zhou, Adhesion effects on spreading of metal powders in selective laser melting, Powder Technol. 363 (2020) 602–610.
[25] L. Wang, Z. Zhou, E. Li, H. Shen, A. Yu, Powder deposition mechanism during powder spreading with different spreader geometries in powder bed fusion additive manufacturing, Powder Technol. 395 (2022) 802–810.
[26] E.L. Li, L. Wang, A.B. Yu, Z.Y. Zhou, A three-phase model for simulation of heat transfer and melt pool behaviour in laser powder bed fusion process, Powder Technol. 381 (2021) 298–312.
[27] E. Li, Z. Zhou, L. Wang, H. Shen, R. Zou, A. Yu, Particle scale modelling of melt pool dynamics and pore formation in selective laser melting additive manufacturing, Powder Technol. 397 (2022).
[28] K.C. Mills, Recommended Values of Thermophysical Properties For Selected Commercial Alloys, Woodhead Publishing, 2002.
[29] G. Welsch, R. Boyer, E.W. Collings, Materials Properties handbook: titanium alloys, ASM international, 1993.
[30] W.A. Ayoola, W.J. Suder, S.W. Williams, Effect of beam shape and spatial energy distribution on weld bead geometry in conduction welding, Opt. Laser Technol. 117 (2019) 280–287.
[31] W.J. Suder, S.W. Williams, Investigation of the effects of basic laser material interaction parameters in laser welding, J. Laser Appl. 24 (2012) 032009.
[32] Y.S. Lee, W. Zhang, Modeling of heat transfer, fluid flow and solidification microstructure of nickel-base superalloy fabricated by laser powder bed fusion, Addit. Manuf. 12 (2016) 178–188.
[33] R. Shi, S.A. Khairallah, T.T. Roehling, T.W. Heo, J.T. McKeown, M.J. Matthews, Microstructural control in metal laser powder bed fusion additive manufacturing using laser beam shaping strategy, Acta Mater. 184 (2020) 284–305.
[34] J.D. Hunt, Steady state columnar and equiaxed growth of dendrites and eutectic, Mater. Sci. Eng. 65 (1984) 75–83.
[35] P.A. Kobryn, S.L. Semiatin, Microstructure and texture evolution during solidification processing of Ti–6Al–4V, J. Mater. Process. Technol. 135 (2003) 330–339.
[36] J. Gockel, J. Beuth, K. Taminger, Integrated control of solidification microstructure and melt pool dimensions in electron beam wire feed additive manufacturing of Ti-6Al-4V, Addit. Manuf. 1 (2014) 119–126.
[37] E. Li, Z. Zhou, L. Wang, R. Zou, A. Yu, Modelling of keyhole dynamics and melt pool flow in laser powder bed fusion process, Powder Technol. (2022) 117262.
[38] C. Kusuma, The effect of laser power and scan speed on melt pool characteristics of pure titanium and Ti-6Al-4V alloy for selective laser melting, (2016).
[39] Z. Yang, A. Bauereiß, M. Markl, C. Körner, Modeling laser beam absorption of metal alloys at high temperatures for selective laser melting, Adv. Eng. Mater. 23 (2021) 2100137.
[40] E. Li, Z. Zhou, L. Wang, R. Zou, A. Yu, Numerical studies of melt pool and gas bubble dynamics in laser powder bed fusion process, Addit. Manuf. 56 (2022) 102913.
[41] A.K. Mishra, A. Kumar, Numerical and experimental analysis of the effect of volumetric energy absorption in powder layer on thermal-fluidic transport in selective laser melting of Ti6Al4V, Opt. Laser Technol. 111 (2019) 227–239.
[42] X. Ji, S. Zhang, Y. Wang, S.Y. Liang, Effect of thermal-fluidic transport on the temperature distribution and the melt pool in laser powder bed fusion of Ti6Al4V, Opt. Laser Technol. 156 (2022) 108587.
[43] D. Zhang, P. Zhang, Z. Liu, Z. Feng, C. Wang, Y. Guo, Thermofluid field of molten pool and its effects during selective laser melting (SLM) of Inconel 718 alloy, Addit. Manuf. 21 (2018) 567–578.
[44] T. Vilaro, C. Colin, J.-D. Bartout, As-fabricated and heat-treated microstructures of the Ti-6Al-4V alloy processed by selective laser melting, Metall. Mater. Trans. A 42 (2011) 3190–3199.
[45] P.A. Kobryn, S.L. Semiatin, The laser additive manufacture of Ti-6Al-4V, JOM 53 (2001) 40–42.
[46] T.T. Roehling, R. Shi, S.A. Khairallah, J.D. Roehling, G.M. Guss, J.T. McKeown, M.J. Matthews, Controlling grain nucleation and morphology by laser beam shaping in metal additive manufacturing, Mater. Des. 195 (2020) 109071.
[47] C.J. Todaro, M.A. Easton, D. Qiu, D. Zhang, M.J. Bermingham, E.W. Lui, M. Brandt, D.H. StJohn, M. Qian, Grain structure control during metal 3D printing by high-intensity ultrasound, Nat. Commun. 11 (2020) 1–9.
[48] M.J. Bermingham, D.H. StJohn, J. Krynen, S. Tedman-Jones, M.S. Dargusch, Promoting the columnar to equiaxed transition and grain refinement of titanium alloys during additive manufacturing, Acta Mater. 168 (2019) 261–274.
[49] M. Qi, S. Huang, Y. Ma, S.S. Youssef, R. Zhang, J. Qiu, J. Lei, R. Yang, Columnar to equiaxed transition during β heat treatment in a near β alloy by laser additive manufacture, J. Mater. Res. Technol. 13 (2021) 1159–1168.